Showcasing research from Professor Arnulf Latz's group, Institute of Engineering Thermodynamics, Department Computational Electrochemistry, German Aerospace Center (DLR), Ulm, Germany.
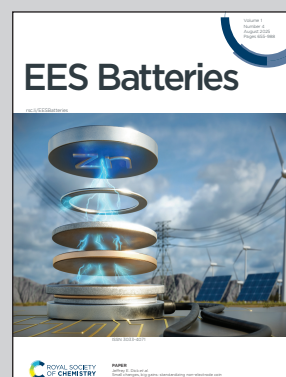
Strategies to spatially guide Li deposition in porous electrodes for high-performance lithium metal batteries

Porous architectures potentially enable safe and stable anode-free Li metal anodes. However, infilling of the pores with Li is always competing with undesired plating on top of the structure, which can lead to problematic dendrite formation. Several sophisticated design strategies aim at a spatial control of Li nucleation and growth. Comprehensive continuum simulations reveal the most effective approaches to ensure a reliable bottom-up infilling of the porous architecture with Li metal during charge. These insights enable to systematically optimize the design of porous architectures and realize practical Li metal anodes.

Image reproduced by permission of Janina Drews, Timo Danner and Arnulf Latz from *EES Batteries*, 2025, **1**, 774.

Cover image partially generated with AI tools.

As featured in:

See Janina Drews *et al.*,
EES Batteries, 2025, **1**, 774.

ROYAL SOCIETY
OF **CHEMISTRY**

rsc.li/EESBatteries

PERSPECTIVE

Strategies to spatially guide Li deposition in porous electrodes for high-performance lithium metal batteries†

Janina Drews, ⓘD *[a,b] Timo Danner ⓘD [a,b] and Arnulf Latz ⓘD [a,b,c]

To exploit the high theoretical energy density of Li metal anodes, critical issues like drastic volume changes and dendritic Li growth need to be overcome. A rational design of the anode is key to enhancing the safety and extending the cycle life of Li metal batteries. Thereby, 3D host architectures are a promising strategy to alleviate volume changes. However, the challenge is to ensure bottom-up infilling and prevent Li deposition and consequent dendrite formation on top of the host structure. This perspective on promising strategies to spatially guide Li deposition analyzes the impact of the structural and physical properties of the host matrix. Extensive parameter studies reveal key strategies to achieve the desired bottom-up infilling and provide a detailed roadmap to effectively design porous host architectures that enable spatially controlled Li deposition.

Broader context

Batteries with a higher energy density are highly attractive, as they promise to improve the performance of our everyday technologies such as electric vehicles and mobile devices. Due to their ultrahigh theoretical energy density, Li metal anodes are regarded as the holy grail in battery research. However, achieving safe and stable cycling of Li metal batteries remains a challenge. Porous structures not only help accommodate volume changes during cycling and facilitate uniform Li deposition but also enable an anode-free cell design without excess metallic lithium, which further optimizes the energy density, improves safety and reduces resource consumption and costs. However, it is challenging to ensure that Li properly infills the porous structure and does not deposit on top. Many promising strategies have been proposed to spatially guide Li deposition. Based on comprehensive simulations in 3D and 1D, this perspective elucidates the most effective approaches towards reliable bottom-up infilling of the porous electrode. This opens up opportunities to systematically optimize the design of porous architectures and realize practical Li metal anodes.

1. Introduction

Batteries have become an important part of our modern everyday life as well as for a fossil fuel-free future. With ongoing technological advancements and the persistent growth of markets for electric vehicles and portable devices, the demand for safe, high-energy-density batteries with excellent rate performance is increasing.[1–4] Since intercalation host materials add significant dead weight to battery cells, employing metal anodes is key to achieving high energy densities. In particular, Li metal-based batteries (LMBs) hold great potential to outperform the state-of-the-art Li-ion battery (LIB) technology with

graphite anodes. A low density, high specific capacity and low redox potential make Li metal an ideal anode for batteries with high energy density.[1,5–7] However, Li plating and stripping lead to massive volume changes, and moreover, Li deposition tends to be inhomogeneous, often resulting in dendrite formation. This not only limits the cycle life of LMBs but also causes a severe safety issue due to the possibility of short-circuiting.[1,5–11]

To overcome the bottleneck of Li metal anodes for practical high-energy-density LMBs, several strategies to prevent dendritic Li growth have been proposed. These include the employment of alloy anodes and extensive electrolyte and interface tailoring. For instance, artificial solid electrolyte interphases (SEIs) and solid-state electrolytes may act as mechanical barriers for dendrite penetration.[6–9,12–17] Micro- or nanostructuring of the anode or current collector is another promising approach since a 3D host matrix additionally enables it to cope with the drastic volume changes during Li plating and stripping. Furthermore, 3D structures provide a larger effective surface area for electrochemical reactions than a Li foil.

[a]*Institute of Engineering Thermodynamics, German Aerospace Center (DLR), Wilhelm-Runge-Straße 10, 89081 Ulm, Germany. E-mail: janina.drews@dlr.de*
[b]*Helmholtz Institute Ulm (HIU), Helmholtzstraße 11, 89081 Ulm, Germany*
[c]*Institute of Electrochemistry, Ulm University (UUlm), Albert-Einstein-Allee 47, 89081 Ulm, Germany*

Thereby the local current density is reduced, which can support more homogeneous growth of Li.[6–8,16,18–24]

However, it is found that, due to ionic transport limitations and the resulting unfavorable electric field distribution, Li predominantly plates on top of the 3D porous structure instead of infilling its internal pores.[24–33] In general, Li nucleation and growth are governed by thermodynamic and kinetic effects, mainly by existing nucleation barriers, local electric potentials and local Li-ion concentrations, which are strongly linked to the structural and physical properties of the porous host framework. Consequently, the rational design of the 3D host architecture is crucial to unleash not only high capacity but also dendrite-free Li deposition and excellent reversibility. For instance, 3D frameworks may comprise porosity and conductivity gradients. This enables the regulation of the local electric potential of the host and the transport of Li^+ cations into the structure, respectively, and consequently, guides Li deposition and promotes the desired bottom-up infilling of the host architectures.[24–26,30,34–37] Moreover, Li nucleation and growth can be spatially controlled by lithiophilic effects. Lithiophilic materials like tin (Sn), silver (Ag), gold (Au), germanium (Ge) or zinc oxide (ZnO) possess no or negligible overpotential for Li nucleation and, consequently, can be employed to introduce preferred nucleation sites.[6,24,25,33,38–46] In general, lithiophilic materials can act as functional coatings on the Li metal anode or planar current collector,[40,47,48] as well as interlayers or seeds within a 3D porous host structure. The latter strategy also allows the design of lithiophilic–lithiophobic gradient electrodes, thereby guiding Li deposition.[6,24,25,30,33,39,40,43,49–51]

All in all, there are many different strategies to prevent dendritic Li growth, which furthermore may be combined with each other.[23,25,27,30,37,42,52,53] This results in endless design possibilities, especially for 3D host matrices.

The aim of this work is to provide a comprehensive perspective on the influence and interplay of the structural and physical properties of the host on the spatial distribution of Li plating. Microstructure-resolved 3D simulations enable detailed insights into structure-related impact factors, while 1D simulations complement and extend the studied parameter space. The influence of the 3D host's porosity, tortuosity, thickness/capacity, surface area and electrical conductivity with and without a lithiophilic interlayer is analyzed in detail. Moreover, diverse combinations of promising design strategies are studied, which provides a better understanding of synergistic effects. Thereby, the most effective design parameters for achieving bottom-up and maximized Li infilling of a porous host anode are identified, providing valuable guidance for the future optimization of the cell designs of LMBs with 3D-structured host matrices.

2. Methodology

2.1. Continuum model and the simulation framework

The basis of the continuum model is a thermodynamically consistent formulation of the transport theory for liquid elec-

trolytes, which is extended with transport in solid materials and electrochemical reactions at their interfaces.[54] Thereby, charge and mass conservation result in a set of coupled partial differential equations (eqn (S1)–(S3)†). This fundamental set of conservation equations is solved numerically in a 3D framework as well as in a 1D framework. The former directly resolves the microstructure of the porous host matrix and, therefore, its impact on transport and heterogeneous reactions. For the separator and the 1D simulations, the effect of the porous geometry is considered implicitly by a volume-averaging method. Thereby, characteristic material properties, namely, porosity ε_e^0 and tortuosity τ are used to effectively scale the transport (eqn (S4)–(S6)†).

The kinetics of Li plating and stripping are described by the common Butler–Volmer equation, which correlates the faradaic current density across the electrode–electrolyte interface i_{se} with the overpotential η (eqn (1)):

$$i_{se} = i_0 \cdot \left[\exp\left(\frac{F}{RT}(1 - \alpha)\eta \right) - \exp\left(-\frac{F}{RT}\alpha\eta \right) \right] \quad (1)$$

F, R, and T are the Faraday constant, the ideal gas constant and the temperature, respectively, and α is the so-called symmetry factor, which describes the relative contributions of stripping and plating to the overall overpotential. Moreover, the exchange current density i_0 is given by the rate constant k_{BV} and the concentrations of the reactants, particularly the concentration of Li^+ in the electrolyte c_e (eqn (2)).

$$i_0 = F \cdot k_{BV} \cdot c_e^{(1-\alpha)} \quad (2)$$

The overpotential η, which controls the electrochemical reaction (eqn (1)), can be described using eqn (3) and denotes the deviation of the potential difference $(\Phi_s - \varphi_e)$ from the equilibrium (U_0):

$$\eta = \Phi_s - \varphi_e - U_0 - (1 - \Theta) \cdot \eta_{nuc} \quad (3)$$

Thereby, Φ_s stands for the electric potential of the solid electrode, φ_e is the electrochemical potential of the electrolyte and U_0 is the open-circuit potential vs. the reference Li/Li^+. Consequently, for Li plating and stripping $U_0 = 0$ V. Moreover, initial Li deposition into a 3D structured host matrix requires overcoming a material-specific barrier, the nucleation overpotential η_{nuc}. This can be considered an additional contribution to the overall overpotential η (eqn (3)). However, subsequent growth of the deposited Li nuclei occurs without the extra overpotential η_{nuc}. Therefore, the nucleation barrier is only taken into account for the part of the surface that is not covered by Li metal (eqn (3)). $0 \leq \Theta \leq 1$ denotes the fractional coverage of the porous electrode with Li, which is described using eqn (4). Thereby, the continuously differentiable power law guarantees the numerical stability of the simulations:

$$\Theta = \frac{\varepsilon_{Li}^4}{\left(0.5 \cdot \varepsilon_{Li,ref}\right)^4 + \varepsilon_{Li}^4} \quad (4)$$

The reference value of the Li volume fraction $\varepsilon_{Li,ref}$ is the main parameter for considering that nucleation and the there-

fore required overpotential η_{nuc} only play a role in the initial deposition phase. For $\varepsilon_{Li} \geq \varepsilon_{Li,ref}$, the surface of the porous host structure is fully covered by plated Li ($\Theta \approx 1$, eqn (4)). Consequently, the barrier for Li nucleation vanishes completely, and η_{nuc} does not contribute to the overpotential for Li deposition η anymore (eqn (3)).

This kinetic model for Li plating with nucleation is implemented in the Battery and Electrochemistry Simulation Tool (BEST) and has been proven to be in good agreement with experimental data.[33] BEST is jointly developed by DLR/HIU and Fraunhofer ITWM Kaiserslautern for physics-based 3D multiscale simulations of LIBs based on the thermodynamically consistent transport theory of Latz et al. (eqn (S1)–(S3)†).[54,55] Thereby, the previously reported model for Li plating and stripping[56] is extended using eqn (3) and (4). To preserve consistency with the work of Hein et al.,[56] eqn (4) is expressed based on the amount of substance n instead of the volume fractions ε. However, the conversion of the reference value $\varepsilon_{Li,ref}$ into its analogue $n_{Li,ref}$ is straightforward.[33]

Since BEST is originally designed to simulate LIBs, the framework does not allow for the resolution of changes in Li metal volume and morphology during the plating and stripping process, and an extension is not straightforward and beyond the scope of this work. Consequently, the 3D simulations can only reasonably depict the very initial Li deposition phase. Still, they track the amount and thickness of Li on the surface, allowing us to identify whether Li preferentially plates at the top or bottom of the structure. We expect that the initial plating phase is decisive for the further growth mechanism.

This can be shown by additionally simulating prolonged Li plating in a homogenized 1D framework, which is implemented in MATLAB[57] and validated by the 3D simulation results. Moreover, simulations in 1D are less time-intensive, allowing for more extensive parameter studies. Therefore, the combination of 1D and 3D simulations enables a comprehensive analysis of the impact of the 3D microstructure as well as the impact of various geometric and physical parameters on the Li infilling of the host structure.

Thereby, the 1D simulations explicitly resolve the change in the Li volume fraction ε_{Li} and the respective differential equation (eqn (5)) is directly coupled to the transport equations for porous media (eqn (S4) and (S5)†), whereby the changing electrolyte volume fraction is calculated according to eqn (7). This approach allows for the depiction of pore clogging by Li deposition and the resulting effects:

$$\frac{\partial \varepsilon_{Li}}{\partial t} = -\frac{M_{Li}}{\rho_{Li}} \cdot a \cdot \frac{i_{se}}{F} \quad (5)$$

M_{Li} and ρ_{Li} denote the molar mass and density of Li metal, respectively, and a is the surface area, which is available for Li plating. Since the microstructure of the porous host matrix cannot be resolved in 1D, the surface area also serves to effectively scale the electrochemical reaction ($i_{se,eff} = a \cdot i_{se}$, eqn (1)). In general, two contributions determine the value of a (eqn (6)). On the one hand, Li can plate on the uncovered surface of the host structure, and on the other hand, plating can take place on the surface of existing Li deposits.

$$a = a_0 \cdot (1 - \Theta) + a_0 \cdot \left(\frac{\varepsilon_{Li}}{\varepsilon_{Li,ref}}\right) \cdot \left(\frac{\varepsilon_e}{\varepsilon_e^0}\right)^{1.5} \quad (6)$$

Thereby, a_0 denotes the surface area of the porous host matrix and ε_e is the electrolyte volume fraction. Its initial value ε_e^0 is given by the porosity of the host structure ($\varepsilon_{Li}^0 = 0$), and subsequently, ε_e can be calculated using eqn (7):

$$\varepsilon_e = \varepsilon_e^0 - \varepsilon_{Li} \quad (7)$$

It should be noted that the description of the surface area a (eqn (6)) is an empirical expression based on the approach of Richter et al.[58] In general, the surface area of the host material decreases with ε_{Li} until it is fully covered with Li ($\Theta = 1$). In contrast, the surface of the Li deposits increases during initial Li plating but decreases later on due to spatial confinement and the beginning of pore clogging.

Since Li deposition can be seen as a competition between nucleation and growth and, moreover, there is always a certain barrier for the formation of new Li nuclei, it needs to be considered that growth may become the dominant mechanism. Thereby, existing Li deposits may extend beyond the control volumes of the spatial discretization, which is required to numerically solve the set of differential equations. Such potential propagation of Li growth is included in the model by introducing the effective value $\varepsilon_{Li,eff}$ (eqn (8)), which replaces ε_{Li} in eqn (4) and (6). Thereby, the effective Li volume fraction $\varepsilon_{Li,eff}$ is given by a weighted mean between the values for ε_{Li} at position x represented by the discrete index ix and its direct neighbors at indices ix − 1 and ix + 1 (eqn (8)). The weighting factors originate from consistently transferring all three dimensions into the 1D model (Fig. S1†).

$$\varepsilon_{Li,eff} = \frac{5\varepsilon_{Li,(ix)} + \varepsilon_{Li,(ix-1)} + \varepsilon_{Li,(ix+1)}}{7} \quad (8)$$

All in all, the presented, generic kinetic model for Li plating based on a nucleation and growth mechanism (eqn (1)–(4)) is incorporated into two different simulation frameworks, which are based on similar thermodynamically consistent transport theory (eqn (S1)–(S6)†). Thereby, BEST enables the spatial resolution of the 3D microstructure of the porous host matrix, while the 1D simulation framework can consider more detailed features of Li growth (eqn (5)–(8)), which are negligible for initial Li plating but become relevant at advanced time steps. Consequently, the combination of 1D and 3D simulations provides a more comprehensive understanding of Li deposition into a porous host architecture, including limitations and effective design strategies.

2.2. Parameterization

All electrolyte transport parameters, namely, the ionic conductivity κ, the diffusion coefficient D, the transference number t_+ and the thermodynamic factor f_{thermo}, are chosen as concentration-dependent functions (Fig. S2†) based on the literature

data for the commonly used bis(trifluoromethane) sulfonimide lithium salt (LiTFSI) dissolved in a 1 : 1 (vol%) mixture of 1,2-dimethoxyethane (DME) and 1,3-dioxolane (DOL).[59,60] The initial electrolyte concentration c_e is 1 M as regularly used in experiments.[13,61–64] Moreover, all simulations are based on the geometric parameters of a typical Celgard separator (Table S2†).

The 3D simulations are based on artificially generated microstructures from Prifling *et al.*,[65,66] whereby six different types of microstructures are analyzed as porous host matrixes for anode-free LMBs: fiber systems, channel systems, spatial stochastic graphs, level sets of Gaussian random fields, level sets of spinodal decomposition and systems of ellipsoids. All simulated porous host architectures were chosen from a data set of 90 000 microstructures based on their type, porosity, geodesic tortuosity, surface area and connectivity. For instance, structures of all different types with close to 90%, 70% and 50% porosity, comparable surface area and comparable tortuosity were selected for analyzing the impact of the microstructure morphology. In all cases, we require connectivity of the solid framework of at least 95% (Table S3†). It should be noted that it is more difficult to find comparable microstructures with high porosity. Therefore, the geometric parameters differ slightly (Table S3†). However, the large number of studied microstructures, which also includes less porous structures with very similar geometric features, enables us to clearly identify qualitative trends. Moreover, fiber structures with 50% porosity, comparable tortuosity, high interconnectivity (>99%) and different surface areas were examined. Additionally, different porous fiber structures with comparable surface area and tortuosity were simulated. For evaluating the influence of tortuosity, the more relevant flux-based tortuosity is determined (Section S1.2†) which strongly correlates with the geodesic tortuosity (Fig. S10c†). Finally, two highly connected fiber structures with different porosities and surface areas were combined into two-layered structures with different ratios of the layers (Table S4†). An overview of all analyzed 3D microstructures including their geometric descriptors and their identifiers can be found in Tables S3 and S4.†

It should be noted that the stochastically generated microstructures from Prifling *et al.* consist of 192_3 voxels, which are scalable and fulfill periodic boundary conditions.[65,66] Consequently, the size of the 3D structure and the voxels has to be chosen reasonably. In general, the voxel size determines the thickness and surface area of the electrode. The corresponding impacts on the simulation results were analyzed carefully (*cf.* section S1.5 of the ESI†). Overall, the effects related to a different thickness clearly dominate and the impact of the voxel size itself is negligible. Additionally, the thickness and porosity of the microstructure determine the capacity of the Li metal anode (Fig. S3†). To obtain 3D microstructures with realistic thickness and capacity, the voxel size was chosen to be 0.25 μm, which corresponds to 48 μm thick host anodes (192^3 voxels). For porosities between 50% and 90%, these microstructures offer a maximum capacity of 5–9 mA h cm^{-2} (Table S5†). However, for practical applications, a comparison

of microstructures with a similar capacity seems more reasonable. Therefore, the 3D microstructures (with 0.25 μm voxel size) were also cut/extended in the through direction to create structures with a capacity of 5 mA h cm^{-2}. The resulting thickness of the different porous host architectures can be found in Fig. S3 and Table S5.†

Li plating on typical host materials like carbon requires overcoming a nucleation barrier of several tens of mV.[38] Unless otherwise stated, a nucleation overpotential of η_{nuc} = 20 mV was chosen (eqn (3)). To simulate a lithiophilic interlayer, the voxels of the surface closest to the current collector were assigned to enable Li deposition without a significant nucleation overpotential ($\eta_{nuc} \approx 0$ V).

For the 1D simulations, the thickness of the host structure is chosen to match 5 mA h cm^{-2}, which corresponds to 48.5 μm for the base porosity of 50% (Table S2†). Dual structures are generated by adding a 5 μm thin interlayer between the current collector and the host architecture. This additional layer is considered to be lithiophilic ($\eta_{nuc} \approx 0$ V) and/or to have a different surface area (Tables S2 and S6†).

All kinetic parameters for Li deposition are chosen based on the literature data and can be found in Table S6.† Details on the estimation, interpretation, and impact of the reference parameter $\varepsilon_{Li,ref}$ and the conversion into $n_{Li,ref}$ are described in previous work.[33] Nevertheless, the sensitivity of the 3D simulation results to $n_{Li,ref}$ is checked, showing that the influence of $n_{Li,ref}$ is very small (<0.5%, Fig. S6†), which is in accordance with the findings on $\varepsilon_{Li,ref}$.[33] Therefore, an educated guess of the order of magnitude of $\varepsilon_{Li,ref}/n_{Li,ref}$ is sufficient.

Moreover, the porous host matrix is considered to be electrically conductive (Table S6†) since typical host materials include carbon and metals like copper or nickel.[8,16,18–22,41,67,68] However, non-conductive structured anodes are also reported in the literature,[8,69,70] and therefore, the electrical conductivity is also varied throughout the simulations. In general, all parameter studies are conducted by varying one parameter of the base parameter set (Tables S2 and S6†) at a time. Despite the electrical conductivity, this includes the 3D microstructure, the existence of a lithiophilic interlayer and the nucleation overpotential η_{nuc} on the porous host. Additionally, the impact of porosity ε_e^0, tortuosity τ, surface area a_0, thickness of the host structure d, electrolyte concentration c_e and symmetry factor of Li deposition α are analyzed.

3. Results and discussion

3.1. Requirements for competitive Li metal host anodes

Introducing a 3D host matrix to accommodate volume changes and reduce the risk of dendritic Li growth is an appealing strategy for producing safe LMBs. However, one has to bear in mind that the additional porous anode structure is inactive and increases the dead weight of the battery cell. To avoid significantly reducing the benefit of LMBs in terms of energy density, the host structure should be as porous and lightweight
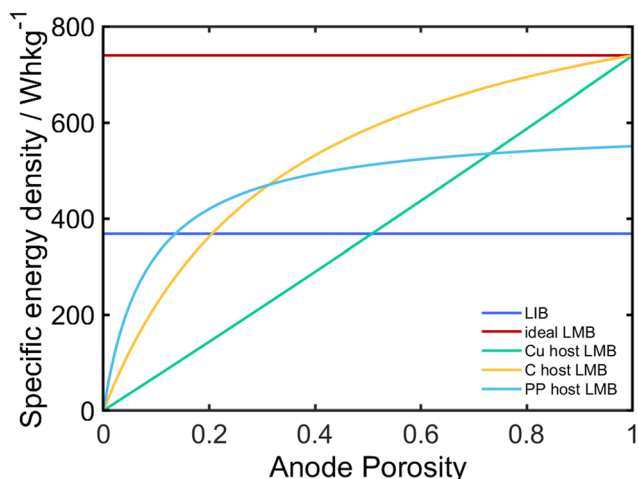
Fig. 1 Specific energy density at the cell level for LIB and LMB full cells with an NMC cathode and 25% excess anodes. Impact of the host anode's porosity for a 5 mA h cm^{-2} cathode. It should be noted that the porosity of the graphite anode (LIB) is not varied. All details on the energy density calculations can be found in the ESI (section S1.3 with eqn (S9)–(S13)†).

as possible (Fig. 1). Consequently, metals like Cu are generally not the ideal material for the 3D host matrix, and Cu-based host LMBs can only be competitive with state-of-the-art LIBs when their porosity is significantly higher than 50% (Fig. 1). Polymers like PP with very low density seem to be promising. However, metal electrodes can act as standalone electrodes. Since polymers are usually non-conductive, an additional current collector is required, which also adds dead weight to the cell and reduces the maximum energy density by more than 100 W h kg^{-1} (light blue line in Fig. 1). Therefore, non-conductive host materials are also not ideal for maximizing the specific energy density of the battery. For typical loadings, carbon-based host matrices hold the greatest potential in terms of energy density, approaching values close to the ideal LMB – already with medium porosity (Fig. 1).

Independent of the choice of host material, the theoretical energy density becomes insignificant as soon as the Li metal does not infill the pores of the 3D matrix and instead tends to deposit on top of it, which potentially causes dendritic growth – a major safety concern. Consequently, ensuring reliable bottom-up infilling of the host architecture is key towards practical LMBs.

3.2. Influence of the 3D microstructure

Systematic micro- and nanostructuring of porous anodes or current collectors is a common strategy to regulate Li deposition and thereby enable safe and durable LMBs.[67,68,70–72] The crucial bottleneck that needs to be overcome is that Li plating is usually more favored on the separator-facing side of the microstructure which prevents the desired bottom-up infilling of the 3D host architecture.[52,56,73] With our 3D simulations, we aim towards a better understanding of the impact of the porous microstructure on the spatial distribution of Li plating.

The ratio between plated Li at the current collector and separator is an indicator of the tendency of infilling in different microstructures. In general, a higher value indicates a beneficial influence, meaning that on-top plating is less dominant and better infilling of the pores is achieved. Fig. 2a and b evaluate the ratio of the mean amount of plated Li on the first and last 5 voxels (1.25 μm) in the through direction after 10 s at 0.1 mA cm^{-2} for six different types of artificial microstructures[65,66] with comparable geometric parameters (Table S3†). Additionally, the distribution of plated Li within the 3D microstructures is shown (Fig. 2c and S7†). No clear trend can be observed and none of the microstructure types is significantly favorable. Instead, the impact of the porosity is much more pronounced, independent of the microstructure type. Consequently, general geometric properties like porosity seem to be remarkably more important than the morphology, such as grains or fibers, of the 3D microstructure itself.

In the next step the impact of the microstructure, that is, porosity, tortuosity and surface area, is analyzed in more detail. Therefore, the ratio of the effective mean values for Li deposition on the current collector and separator sides of all previously analyzed microstructures (Fig. 2) is plotted as a function of these three geometric parameters (Fig. 3). This illustration clearly shows that microstructures with comparable structural properties were chosen to study the influence of the microstructure type. To completely cover the parameter space, additional fiber structures were selected for simulating Li plating in 3D (Fig. 3). Thereby, fiber systems with similar porosity but different surface areas as well as structures with different porosities and similar surface areas were chosen so that the observed trends can explicitly be assigned to one of these geometric parameters (Fig. S11†). It should be noted that there is an inherent correlation between porosity and tortuosity. In general, more porous structures tend to be less tortuous (Fig. S12†). However, clear trends can be identified (Fig. 3). As expected, a higher porosity and/or a lower tortuosity supports Li deposition on the current collector side, as the transport of Li$^+$ ions through the electrolyte-filled pores is less hindered. This effect is even more pronounced for microstructures with similar capacity, as hosts with higher porosity need to be thinner and therefore reduce the transport pathway to the current collector side (Fig. S4a†). Nevertheless, ensuring fast transport is not sufficient to suppress the undesired on-top plating. For all microstructures analyzed, the Li plating ratio on the current collector and separator sides is significantly lower than 1 (Fig. 3). This is also true at the very beginning of the simulation after 1 s at 0.1 mA cm^{-2} (Fig. S8†) and indicates that Li nucleation preferentially occurs on the separator side and thus on-top plating is always dominating. The main reason therefore is that the availability of Li$^+$ is generally higher on the separator side of the structure, leading to a lower barrier for Li deposition.

Interestingly, increasing the surface area does not seem to be a successful strategy for promoting a bottom-up infilling of the structure, and rather it facilitates on-top plating (Fig. 3c and S11b†). However, the influence of the overall surface area
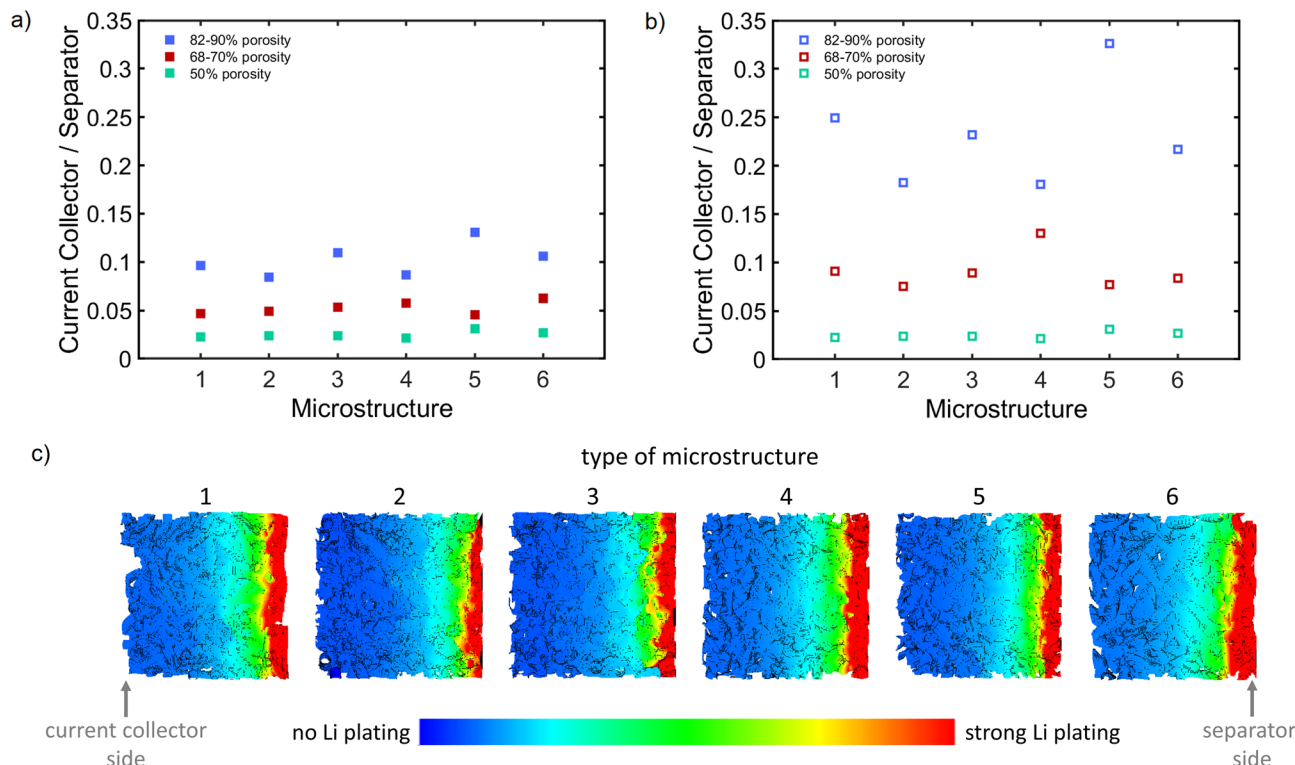
Fig. 2 Influence of the type of microstructure (1 = fiber system, 2 = channel system, 3 = spatial stochastic graph, 4 = level set of a Gaussian random field, 5 = level set of spinodal decomposition, and 6 = ellipsoids; *cf.* Table S3†) on the ratio of the effective, mean amount of Li plating on the current collector and separator sides of microstructures with similar thickness (a) and similar capacity (b) after 10 s at 0.1 mA cm^{-2}. The corresponding distribution of plated Li for microstructures with 70% porosity and similar thickness is shown at the bottom (c). The view is from the side in the through direction. The current collector is located on the left side, while the separator is beginning on the right. An extended figure including all microstructure types and porosities with similar thickness and capacity can be found in the ESI (Fig. S7†).
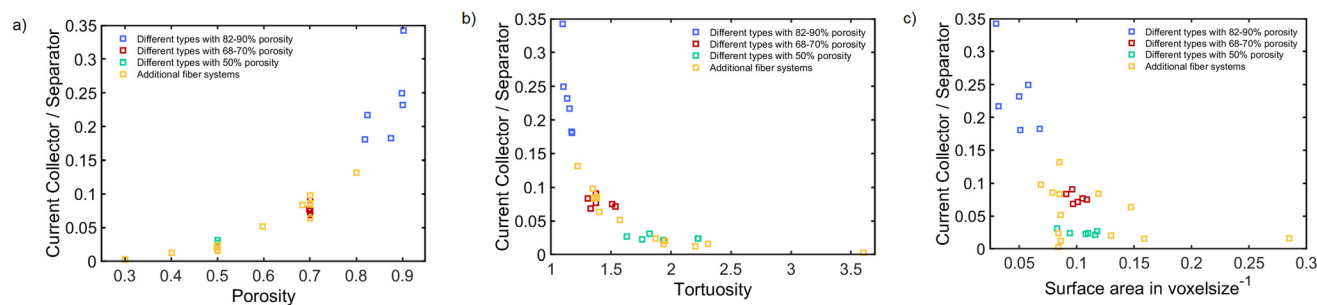
Fig. 3 Influence of the porosity (a), tortuosity (b) and surface area (c) of all analyzed 3D microstructures (*cf.* Table S3†) on the ratio of the effective, mean amount of Li plating on the current collector and separator sides of microstructures with similar capacity after 10 s at 0.1 mA cm^{-2}. Analogue graphs for microstructures with similar thickness as well as the Li distribution after 1 s at 0.1 mA cm^{-2} can be found in the ESI (Fig. S8 and S9†).

is found to be very small especially when compared to the influence of porosity (Fig. S10†). It should be noted that a higher surface area and the resulting reduced local current density may be beneficial for enhancing more homogeneous Li deposition, consequently avoiding dendrite formation.[23,24] Still, it does not provide spatial guidance and therefore does not support the infilling of a 3D architecture with Li. This observation is consistent with the results from analyzing the impact of the voxel size (Fig. S4b and e and Section S1.5†).

Moreover, the slight negative effect of a high surface area seems to be more pronounced for highly porous structures (Fig. S11b†). Additionally, one should bear in mind that, in general, a larger surface area may enhance undesired side reactions. Consequently, the choice of 3D host structures with an especially high surface area is not a promising strategy for producing practical LMBs. It should be noted that, in contrast, a gradient in surface area can enable spatial guidance, which is shown in the subsequent section.

Regarding the correlation between porosity and tortuosity (Fig. S12†), it can be seen that the different types of microstructures tend to show higher or lower tortuosity at similar porosity. Thereby, fiber systems and ellipsoids seem to be inherently less tortuous than the other types of microstructures, which in principle could be an advantage (Fig. 3). However, for higher porous structures, this trend becomes less pronounced, and overall, Fig. S12† supports the previous finding (Fig. 2) that a higher porosity is more relevant than the type of microstructure. Despite the rather small impact of the microstructure type, fiber systems generally seem to be a good choice for a host architecture, and therefore, all further analyses are based on fiber structures.

Since the influence of the detailed 3D microstructure is found to be negligible (Fig. 2) and the impact of more general structural parameters like porosity is dominating, simulations with a homogenized 1D model can be considered to be a suitable approach to study deep charge and discharge cycles. Since 1D simulations are computationally less expensive, more extensive parameter studies are possible. Additionally, the propagation of Li growth can easily be considered in the 1D framework (eqn (8)) so that simulations beyond the initial plating phase are reasonable. Consequently, 1D simulations complement the structure-resolved simulations and help validate that the location of the early Li nuclei – which is analyzed in 3D – is actually guiding the growth mechanism (on-top *vs.* bottom-up).

The 1D parameter studies regarding the influence of porosity, tortuosity and surface area (Fig. S26†) are consistent with the 3D simulation results (Fig. 3 and S11†). A higher surface area of the host architecture generally favors pore clogging and on-top plating (Fig. S26c and f†). In contrast, more porous and less tortuous matrices are found to be beneficial for achieving infilling of the pores. Nevertheless, enhanced transport alone is not able to prevent Li deposition from dominating near the surface of the host structure, eventually leading to pore clogging and consequent on-top plating (Fig. S26a, b, d and e†). As expected, this undesired effect is intensified when a higher current density is applied. While striving for highly porous host structures is a common strategy to maximize the energy density of the anode, tortuosity is often a neglected design parameter. Since it correlates with porosity (Fig. S12†), the tortuosity is also lowered by choosing a highly porous host. However, simulations show that the beneficial effect of low tortuosity is disproportionately high, leading to significant differences between host structures with low or very low tortuosity (Fig. S26b and e†). Consequently, to achieve good infilling of the porous host, minimizing tortuosity has to go hand in hand with maximizing the porosity of the microstructure. Thereby, the plating behavior is significantly more sensitive towards very low tortuosity than towards very high porosity (Fig. 3a and b and S26d, e†). This becomes increasingly prominent for host structures with high pore capacities and operation at high current densities (Fig. S28†). Nevertheless, even an ideal microstructure with minimized tortuosity ($\tau = 1$) as well as a very high porosity (90%) always shows more pronounced plating at the separator side after a quite low amount of the pore capacity is filled (Fig. S27†). This simulation result is in agreement with experimental measurements, which observed significant on-top plating even on a low-tortuosity 3D host consisting of vertically aligned nanofibers after an infilling of *ca.* 30% of the pore capacity.[32] Altogether, microstructures that enable ideal transport in the electrolyte (low tortuosity, high porosity) are beneficial and can significantly postpone pore-clogging and consequent on-top plating, but they are not able to initiate the desired bottom-up infilling of the porous host.

3.3. Influence of surface area and porosity gradients

Gradient structures are another strategy to regulate Li plating.[25,34] On the structural level, porosity and surface area are the basis for designing gradient electrodes. A higher porosity on the separator side ensures sufficiently fast Li$^+$ transport into the pores of the microstructure, while a high surface area on the current collector side is supposed to locally enhance the interfacial activity and, thereby, promote Li nucleation and subsequent upward growth. To simulate such gradient systems, two selected 3D microstructures were combined into dual-layer structures with different ratios of the two layers. Thereby, gradients in porosity and/or surface area are introduced. The layer at the separator side (layer 2) possesses the higher porosity and/or the lower surface area, while the layer facing towards the current collector (layer 1) is less porous and/or has the higher surface area (Table S4†). Our simulations predict that such a dual-layer system can significantly impact the spatial distribution of Li plating (Fig. 4). Interestingly, a host anode with a porosity gradient (layer 1 ≤ 50%) shows slightly more Li plating at the current collector side than a highly porous microstructure (Fig. 4a). However, a porosity gradient alone cannot prevent on-top plating.

In contrast, a gradient in surface area may initiate bottom-up infilling. As expected, this effect is more pronounced for larger gradients in surface area (Fig. S13†). Thereby, the surface area at the current collector side should at least be 2–3 times larger than at the separator side. Moreover, the porosity has an impact on the effectiveness of the surface area gradient. More porous structures enable faster transport and thereby significantly enhance the beneficial effect of the gradient in surface area. Consequently, a combined gradient structure with a higher surface area at the current collector side and a higher porosity at the separator side is most effective in promoting Li nucleation and growth at the bottom of the host architecture (Fig. 4a). It should be noted that structures with medium porosity in principle are able to provide a significantly higher surface area than highly porous microstructures.[65] Consequently, a larger gradient in surface area can be reached when the porosity of layer 1 at the current collector side is not as high as possible. Meanwhile, a high porosity in layer 2 at the separator side ensures good transport of Li$^+$ ions into the host architecture. Therefore, a microstructure with both – a gradient in surface area and in porosity – is a promising approach to enhance bottom-up infilling, especially for a very thin layer at the current collector side (Fig. 4) and thin electro-
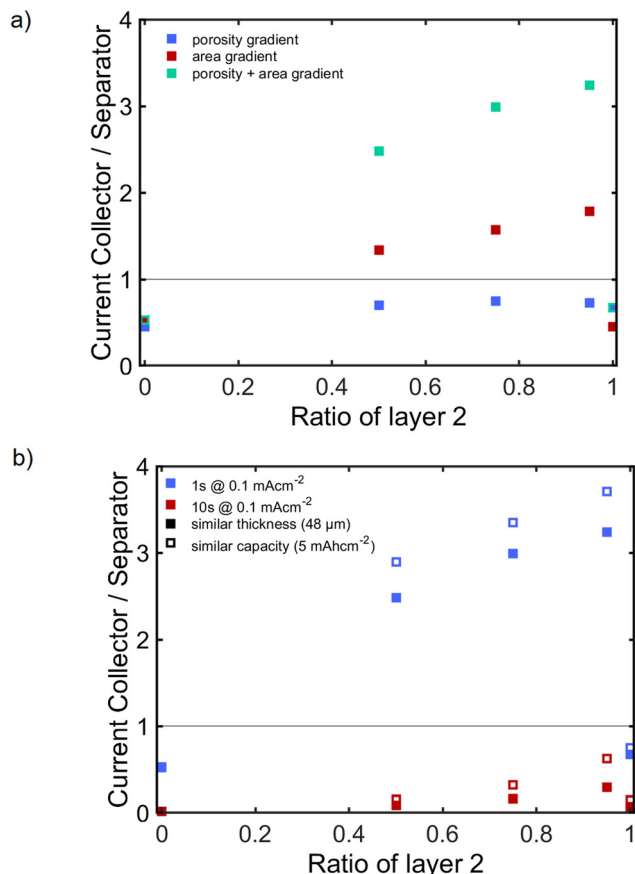
Fig. 4 Influence of a dual-layer structure (layer 1 = current collector side and layer 2 = separator side; train 11 635, train 44 842 and train 27 264; *cf.* Table S4†) on the ratio of the effective, mean amount of Li plating on the current collector and separator sides of the microstructures. (a) Impact of a gradient in porosity (layer 1: low porosity and/or high surface area and layer 2: high porosity and/or low surface area) on microstructures with similar thickness after 1 s at 0.1 mA cm⁻². (b) Impact of a combined porosity and surface area gradient on microstructures with similar thickness and similar capacity after 1 s and 10 s at 0.1 mA cm⁻². The layers consist of a low-porosity (50%) microstructure with a high surface area at the current collector side (layer 1) and a highly porous (90%) microstructure with a low surface area at the separator side (layer 2).

des (Fig. S14†). Thereby, a thinner layer 1 can induce more precise spatial guidance for Li nucleation, while a thin electrode supports sufficient ionic transport, thereby promoting the subsequent growth of the Li nuclei. For all simulated dual-layer structures (layer 1 ≤ 50%), the ratio of plated Li on the current collector and separator side is higher compared to the respective individual single-layer microstructures. This effect is most significant not only for a structure with a combined porosity and surface area gradient (Fig. 4a) but also at the very beginning after 1 s at 0.1 mA cm⁻² (Fig. 4b). Interestingly, at this stage, Li plating on the current collector side dominates whereby up to 4 times more Li deposits at the bottom of the porous host (Fig. 4). It should be noted that for none of the analyzed (single-layer) microstructures as well as none of the dual-layer structures with just a porosity gradient, a plating

ratio >1 was observed (Fig. S8† and Fig. 4a). In contrast, a gradient in surface area (especially combined with a gradient in porosity) is able to clearly initiate Li nucleation at the current collector side. However, these initial Li nuclei do not appear to grow significantly within the next few seconds; instead, Li nucleates and grows on the separator side (Fig. 4b). Still after 10 s at 0.1 mA cm⁻², a thin interlayer with a higher surface area leads to significantly more Li deposition at the current collector side than all other simulated structures (Fig. 3 and 4).

Since the beneficial effect of the surface area gradient seems to fade with time, the results from the 1D simulations, which can cover longer time scales, become appealing. Interestingly, the effect of a higher surface area close to the current collector is found to be very impactful in the 1D simulations (Fig. S29a and d†). Since it can be expected that plating will initially increase the available surface area, the spatially guiding effect of a surface area gradient can be considered as self-reinforcing. While this effect is empirically considered in the 1D simulations (eqn (6)), it is neglected in 3D for computational reasons. Consequently, the beneficial impact of a surface area gradient is underestimated in 3D, while the empirical approach might overestimate the self-enhancement in 1D. All in all, a dual-layer system only based on layers with the different surface areas can initiate and significantly favor, but may not guarantee, the continued bottom-up infilling of the structure, especially at high current densities (Fig. S30a and d†).

Overall, a highly porous host structure and the introduction of a surface area gradient by a thin interlayer with a few times larger surface area are the most effective design options at the microstructure level. In general, transport limitations may be avoided by using a more porous and less tortuous structure. However, even a highly porous structure is not able to induce preferred Li plating at the bottom of the host architecture. In contrast, a gradient in surface area can clearly support Li nucleation at the current collector side. Nevertheless, subsequent upward growth is not ensured and instead Li deposition at the separator side might still dominate after a while (Fig. 4b and Fig. S30a and d†). To guarantee the bottom-up infilling of the porous host, additional strategies are required.

3.4.   Influence of the electrical conductivity of the host architecture

Material-specific properties of the 3D host architecture, namely, its electrical conductivity and its lithophilicity, also impact local Li plating. For conductive host materials, the transport of electrons is significantly faster than the transport of Li⁺ ions in the electrolyte-filled pores of the electrode. Therefore, the ionic transport is the limiting step of the electrochemical reaction, leading to a potential distribution that always favors Li deposition on top of the porous structure. In general, the barrier for a bottom-up infilling is always higher when Li⁺ transport within the electrolyte is the slowest step. In contrast, Li deposition close to the current collector is preferred when the availability of electrons is controlling the

reaction rate. Consequently, slowing down the electronic transport by choosing a host material with low conductivity can be a successful strategy to make Li nucleation close to the current collector and subsequent bottom-up growth more favorable (Fig. 5 and S15†).

As expected, simulations clearly show that Li deposition on a conductive microstructure starts from the separator side, leading to an undesired on-top plating. A reduced electrical conductivity is able to initiate Li deposition close to the current collector since the availability of electrons becomes the dominant barrier. However, the build-up of the concentration gradient can compensate for this initially positive effect of moderate conductivity so that on-top plating still becomes prominent after a short time. Only host materials with very low conductivity can fully suppress Li plating at the separator side (Fig. 5 and S15†). Thereby, the effective ionic transport significantly impacts the maximum tolerable electrical conductivity of the porous host at which the Li deposition behavior changes from on-top plating to bottom-up infilling. Highly porous matrices may be several orders of magnitude more conductive while providing the same ratio of plating at the current collector and separator. Enhancing the ionic transport in the electrolyte and reducing the conductivity of the electrode have to be seen as complementary strategies. However, in contrast to lowering the electrical conductivity of the host architecture, ensuring fast ionic transport is not able to initiate bottom-up infilling on its own (Fig. 3). Nevertheless, it significantly facilitates the subsequent bottom-up filling, and therefore, the initiating force – in this case, the lowered conductivity of the host matrix – needs to be less strong (Fig. 5). A similar effect is observed for a host structure with a gradient in porosity and surface area (Fig. S16†). However, with decreasing conductivity, the beneficial effect of the gradient structure compared to the highly porous (90%) architecture vanishes.

The 1D simulations confirm that a low-conductivity host material is a very effective strategy to completely suppress the safety concerning on-top plating independent of the applied current density (Fig. S29b, e and Fig. S30b, e†). Also for increasing the capacity of the porous anode, a low electrical conductivity is found to be a very successful strategy to prevent pore clogging and on-top plating (Fig. S33†).

However, one should bear in mind that lower-conductivity substrates bring the risk that parts of the deposited Li remain electrically unconnected during stripping, which can strongly limit battery performance. Another negative side effect of low-conductivity host structures is that the effective active surface area is significantly reduced (Fig. 5), leading to higher local currents and overpotentials, which finally, reduce the accessible energy density. Although a lowered surface area can slightly promote pore infilling (Fig. 3c), it also leads to higher overpo-
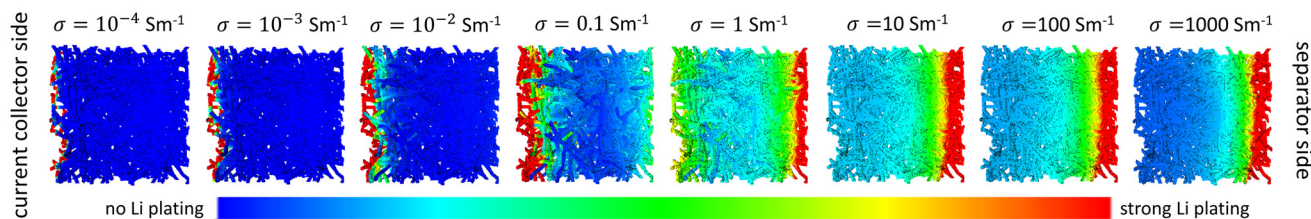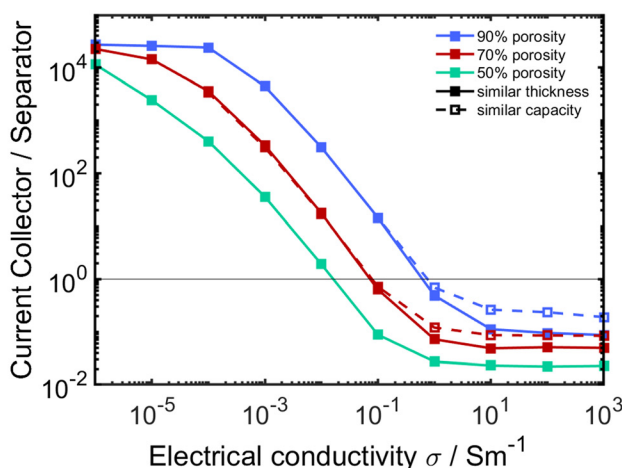
Fig. 5 Top: influence of electrical conductivity on the ratio of the effective, mean amount of Li plating on the current collector and separator sides in microstructures with different porosities (train 11 635, train 5481, and train 44 842; cf. Table S3†) but similar thickness/capacity after 10 s at 0.1 mA cm^{-2}. An extended figure which additionally includes a dual-layer structure with a surface area and porosity gradient can be found in the ESI (Fig. S16†). Bottom: the amount of plated Li on a highly porous (90%) fiber system (train 11 635, cf. Table S3†) with electrical conductivities of $\sigma = 10^{-4}$–10^3 S m^{-1} after 10 s at 0.1 mA cm^{-2}. The shown view is from the side in the through direction. The current collector is located on the left side, while the separator is beginning on the right. An extended figure including all three structures with different porosities can be found in the ESI (Fig. S15†).

tentials for the electrochemical reaction and may impact the morphology of the Li deposits. To avoid the formation of dead Li and excessive reduction of the active surface, it is beneficial for making the host architectures as conductive as possible, which has to go hand in hand with accelerating ionic transport.

Moreover, the introduction of a conductivity gradient might be a beneficial strategy since a non-conductive host matrix cannot act as a current collector, and an additional metal foil is required, which significantly reduces the achievable energy density (Fig. 1). Therefore, a dual-layer system consisting of a thin free-standing, porous layer of a conductive material like carbon or metal and a less conductive porous main layer can be a successful approach. 1D simulations show that such a gradient system behaves very similarly to the system with overall lowered conductivity with a slightly higher tendency towards on-top plating at low current densities and a slightly better suppression of on-top plating at high current densities (Fig. S29–S31†). Nevertheless, tuning the electrical conductivity has to be regarded as a compromise.

3.5. Influence of lithiophilicity gradients

Since low-conductive hosts may lead to the formation of dead Li, another promising approach is to spatially guide Li deposition by the lithiophilicity of the 3D host architecture. The term lithiophilicity describes that materials show specific overpotentials for Li nucleation which for instance depends on the lattice mismatch with the crystal structure of Li. Thereby, lithiophobic materials possess a high barrier to forming Li nuclei, while lithiophilic materials allow Li deposition without a significant nucleation overpotential ($\eta_{nuc} \approx 0$ V).

It should be noted that the lithiophilicity of the host structure in general does not have a significant impact on the Li deposition behavior, and strong on-top plating occurs independent of η_{nuc} (Fig. S17†). However, a gradient in lithiophilicity can effectively induce the infilling of the pores (Fig. 6). Thereby, a lithiophilic interlayer between the current collector and the lithiophobic main matrix introduces preferred nucleation sites, which make Li nucleation at the bottom of the porous host matrix more favorable. However, a sufficiently high gradient in lithiophilicity is required to ensure the subsequent upward growth and prevent later nucleation at the separator side. This is especially true for operations at higher current densities and less porous host materials (Fig. S29c, f and Fig. S30c, f†). Thereby, the effect of a lithiophilic interlayer can significantly be supported by good ionic transport in the electrolyte. The build-up of concentration gradients always favors Li nucleation and growth on top of the porous structure, thereby, counteracting the driving force of the lithiophilic interlayer. It can clearly be seen that the beneficial effect of the same gradient in lithiophilicity is more pronounced for host architectures with higher porosity (Fig. 6 and S18†). Both – 3D and 1D – simulations indicate that a lithiophilicity gradient of *ca.* 50 mV is required to fully initiate and maintain the bottom-up infilling at 0.1 mA h cm^{-1} for matrices with 50% porosity, while the value decreases to 30–40 mV for the highly

porous (90%) microstructure (Fig. S18 and S29f†). It should be noted that the practical magnitude of a lithiophilicity gradient is limited. Typical host materials like C or Cu possess a barrier of ≈20–30 mV for Li nucleation, while very lithiophilic materials do not show such a barrier at all ($\eta_{nuc} = 0$ V).[38] Consequently, the easily achievable gradients in lithiophilicity may not be sufficient to ensure bottom-up infilling especially at higher current densities.

However, the combination of the lithiophilic interlayer with a gradient in porosity and surface area can also enhance the spatial guiding effect (Fig. S19†). As observed before, the effect of the surface area gradient is quite pronounced in the initial plating phase (after 1 s at 0.1 mA cm^{-2}) and fades with time, while the 1D simulations imply a significantly more beneficial effect (Fig. S33†) Particularly for very small lithiophilicity gradients, an additional surface area/porosity gradient can favor the desired bottom-up infilling of the pores. The combination of a lithiophilicity gradient with a less conductive porous host is also beneficial (Fig. S20, S21 and S33†). Such synergistic effects can be key towards reliable spatial control of Li plating.

Moreover, the amount and spatial distribution of the lithiophilic sites can play a role (Fig. S22–S25†). Interestingly, for small gradients in lithiophilicity, a lower number of lithiophilic sites seems to be slightly preferential (Fig. S22†). However, a higher amount of lithiophilic material always reduces the lithiophilicity gradient which is required to completely change from on-top plating to bottom-up infilling (Fig. S23†). Thereby, a limiting behaviour is observed. A certain number of lithiophilic sites is required to effectively induce the desired bottom-up infilling, while an even higher amount of lithiophilic material will not have a significant additional beneficial impact. It should be noted that the amount and morphology of lithiophilic material determine the active surface area. More lithiophilic sites can enhance the available surface area and therefore reduce the local current densities. Consequently, the overpotential for Li deposition is lowered, and plating at the lithiophilic sites becomes even more favorable. Therefore, on-top plating can be suppressed more effectively when more lithiophilic material is available in the interlayer.

To have the strongest spatially guiding effect, the lithiophilic material has to be located close to the current collector. However, it can be seen that when the lithiophilic sites cover a higher depth into the main structure, the initial on-top plating can be suppressed more effectively. This beneficial effect vanishes when the lithiophilic sites are located in more than 50% of the porous matrix (Fig. S24 and S25†). Since lithiophilic sites which are located inside the porous structure will cause preferential Li nucleation and growth not only at the bottom but also more toward the middle of the host matrix, it has to be expected that complete infilling of the pores close to the current collector will be more difficult due to pore clogging. Therefore, a higher depth of the lithiophilic material can be favorable in the initial phase but not for prolonged Li deposition. However, the differences between the analyzed depths of the lithiophilic material are not very pronounced and the number of lithiophilic sites has a significantly stronger impact
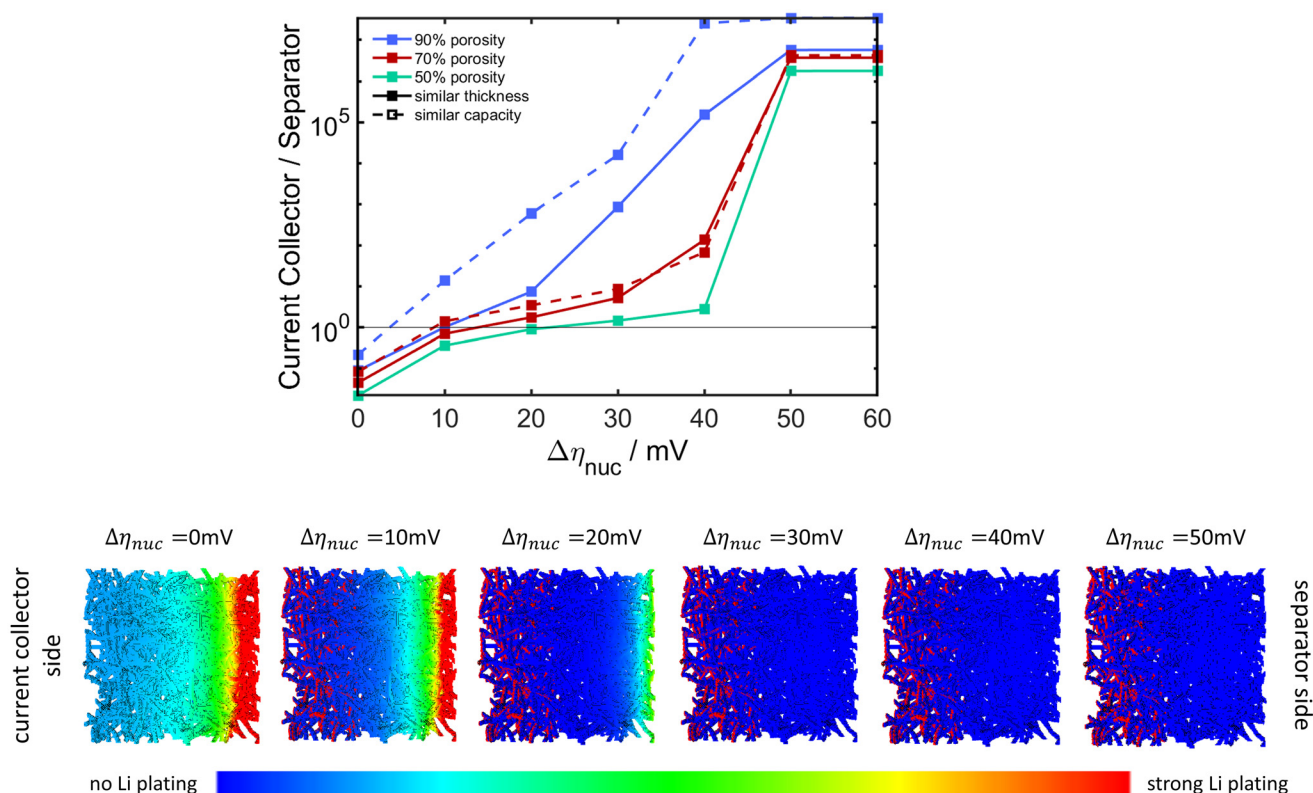
Fig. 6 Top: influence of a gradient in lithiophilicity on the ratio of the effective, mean amount of Li plating on the current collector and separator sides of different porous microstructures (train 11 635, train 5481, and train 44 842; *cf*. Table S3†) with similar thickness and similar capacity after 10 s at 0.1 mA cm^{-2}. An extended figure which additionally includes a dual-layer structure with a surface area and porosity gradient can be found in the ESI (Fig. S19†). Bottom: the amount of plated Li on a highly porous (90%) fiber system with different lithiophilicity (train 11 635; *cf*. Table S3†) in combination with a thin lithiophilic interlayer (η_{nuc} = 0 V) after 10 s at 0.1 mA cm^{-2}. The shown view is from the side in the through direction. The current collector is located on the left side, while the separator is beginning on the right. An extended figure including all three structures with different porosities can be found in the ESI (Fig. S18†).

on the spatial guiding effect. Consequently, it is important to supply enough nucleation sites that are located at the bottom of the porous host architecture. Therefore, one promising strategy is to grow lithiophilic nanowires on one side of the porous host matrix. Thereby, a gradient in lithiophilicity and surface area is introduced at the same time, which can successfully unlock the bottom-up infilling.[33]

3.6. Synergistic effects

In general, one has to differentiate between design strategies that can spatially guide Li nucleation (initiation) and strategies that support the subsequent directed growth (propagation) but are not able to induce a driving force for local Li deposition at the current collector side. Thereby, initiating and propagating factors act synergistically. With enhanced ionic transport in the electrolyte, the initiating driving force can be less strong to reliably suppress on-top plating. Thereby, a low tortuosity is even more beneficial than a high porosity (Fig. S26 and S32†). It should be noted that the choice of electrolyte and separator also impacts ionic transport. Therefore, an effect comparable to that of the porosity and tortuosity of the anode host matrix can be expected. An optimized electrolyte may significantly

support the infilling of the anode pores with Li but may not initiate preferred Li nucleation at the current collector side.

Moreover, the different initiating effects also act synergistically (Fig. S34†). By combining two guiding effects, the two individual driving forces need to be less strong. Thereby, a lithiophilic interlayer with a higher surface area seems to be the most effective (Fig. S34†). The required gradient in lithiophilicity to change from on-top plating to bottom-up infilling is very strongly reduced when the surface area of the lithiophilic interlayer is only twice as high as that of the main structure (Fig. 7). At 0.1 mA cm^{-2}, the lithiophilicity gradient for a 50% porous microstructure can be 5 times lower: 10 mV instead of 50 mV. Even for operation at higher current densities, the beneficial impact of a lithiophilic interlayer with a slightly higher surface area is still remarkable. Interestingly, the surface area gradient does not need to be very pronounced to significantly support the spatially guiding effect of the lithiophilicity gradient (Fig. 7). In contrast a more than 5-fold surface area of the lithiophilic interlayer has no further influence on the required lithiophilicity gradient. Consequently, it is not required to put effort into maximizing the surface area of the lithiophilic interlayer. Instead it is more important to optimize the ionic trans-
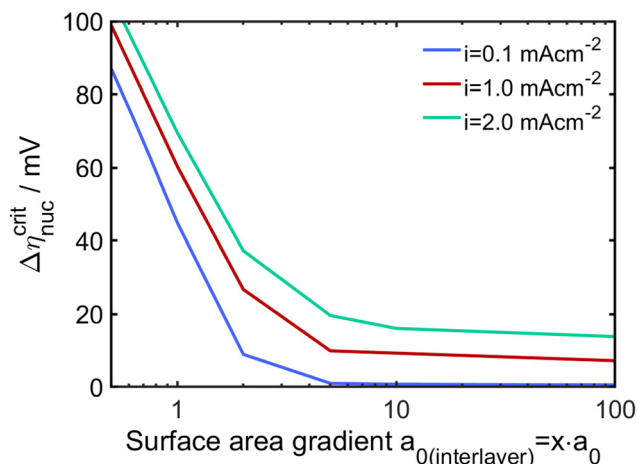
Fig. 7 Synergistic effects between a lithiophilic interlayer (5 μm) and a surface area gradient. The critical gradient in lithiophilicity $\Delta\eta_{nuc}^{crit}$ is required to change from on-top to complete bottom-up infilling for a capacity of 4 mA h cm^{-2}.

port in the electrolyte. Therefore, the combination of a highly porous, low tortuosity host matrix and a lithiophilic interlayer with a moderately larger surface area at the bottom of the porous microstructure is the most promising strategy to effectively avoid undesired on-top plating.

4. Conclusions

In summary, the extended models used to describe Li deposition provide detailed insights into the spatial preferences of Li nucleation and growth. Thereby, simulations in 3D and 1D complement and validate each other and identify different design strategies to spatially control Li plating. Hence, our detailed study can act as a useful guide for the effective design of LMBs with structured anodes.

In general, one has to differentiate between initiating and propagating effects. Avoiding transport limitations, for instance, using a more porous and less tortuous microstructure, is very important but belongs to the latter category. Sufficiently fast transport through the pores of the 3D host architectures is one requirement for achieving reliable bottom-up growth of Li. However, it is not sufficient to effectively avoid on-top plating. This is true for all strategies that only affect the microstructure of the host. Preferred nucleation at the bottom of the porous host matrix needs to be initiated by a physical driving force. Such spatial control of Li deposition can be realized by a balanced reduction of the anode's electrical conductivity or by strategically locating lithiophilic sites into a lithiophobic matrix. Therefore, the combination of lithiophilicity and surface area gradients with a highly porous host matrix is most effective to initiate and ensure the bottom-up infilling of the porous microstructure also at high current densities. Such an ideal combination of different design strategies is key towards the spatial control

of Li nucleation and growth, which is an important step towards realizing safe and stable LMBs.

Data availability

The data supporting this article have been included as part of the ESI.†

Conflicts of interest

There are no conflicts to declare.

Acknowledgements

References

1 J.-M. Tarascon and M. Armand, *Nature*, 2001, **414**, 359–367.
2 Y. Liang, C.-Z. Zhao, H. Yuan, Y. Chen, W. Zhang, J.-Q. Huang, D. Yu, Y. Liu, M.-M. Titirici, Y.-L. Chueh, H. Yu and Q. Zhang, *InfoMat*, 2019, **1**, 6–32.
3 R. Schmuch, R. Wagner, G. Hörpel, T. Placke and M. Winter, *Nat. Energy*, 2018, **3**, 267–278.
4 J. Deng, C. Bae, A. Denlinger and T. Miller, *Joule*, 2020, **4**, 511–515.
5 J. W. Choi and D. Aurbach, *Nat. Rev. Mater.*, 2016, **1**, 16013.
6 D.-H. Liu, Z. Bai, M. Li, A. Yu, D. Luo, W. Liu, L. Yang, J. Lu, K. Amine and Z. Chen, *Chem. Soc. Rev.*, 2020, **49**, 5407–5445.
7 W. Xu, J. Wang, F. Ding, X. Chen, E. Nasybulin, Y. Zhang and J.-G. Zhang, *Energy Environ. Sci.*, 2014, **7**, 513–537.
8 X.-B. Cheng, R. Zhang, C.-Z. Zhao and Q. Zhang, *Chem. Rev.*, 2017, **117**, 10403–10473.
9 Y. Guo, H. Li and T. Zhai, *Adv. Mater.*, 2017, **29**, 1700007.
10 C. Fang, X. Wang and Y. S. Meng, *Trends Chem.*, 2019, **1**, 152–158.
11 A. Hagopian, M.-L. Doublet and J.-S. Filhol, *Energy Environ. Sci.*, 2020, **13**, 5186–5197.
12 S. Li, Z. Luo, L. Li, J. Hu, G. Zou, H. Hou and X. Ji, *Energy Storage Mater.*, 2020, **32**, 306–319.
13 D. Kang, M. Xiao and J. P. Lemmon, *Batteries Supercaps*, 2021, **4**, 445–455.
14 A. Varzi, R. Raccichini, S. Passerini and B. Scrosati, *J. Mater. Chem. A*, 2016, **4**, 17251–17259.
15 T. Krauskopf, F. H. Richter, W. G. Zeier and J. Janek, *Chem. Rev.*, 2020, **120**, 7745–7794.

16 R. Pathak, K. Chen, F. Wu, A. U. Mane, R. V. Bugga, J. W. Elam, Q. Qiao and Y. Zhou, *Energy Storage Mater.*, 2021, **41**, 448–465.

17 T. Naren, R. Jiang, G.-C. Kuang, L. Zhou and L. Chen, *ChemSusChem*, 2024, **17**, e202301228.

18 C.-P. Yang, Y.-X. Yin, S.-F. Zhang, N.-W. Li and Y.-G. Guo, *Nat. Commun.*, 2015, **6**, 8058.

19 D. Li, B. Chen, H. Hu and W.-Y. Lai, *Adv. Sustainable Syst.*, 2022, **6**, 2200010.

20 D. Li, H. Hu, B. Chen and W.-Y. Lai, *Small*, 2022, **18**, 2200010.

21 J.-Y. Eom, S. H. Choi, J.-H. Kang, G. H. Eom, J. Moon and M.-S. Park, *ACS Appl. Energy Mater.*, 2021, **4**, 1936–1941.

22 X. He, K. Zhang, Z. Zhu, Z. Tong and X. Liang, *Chem. Soc. Rev.*, 2024, **53**, 9–24.

23 G.-D. Yang, Y. Liu, X. Ji, S.-M. Zhou, Z. Wang and H.-Z. Sun, *Chem. – Eur. J.*, 2024, **30**, e202304152.

24 X. Wang, Z. Chen, K. Jiang, M. Chen and S. Passerini, *Adv. Energy Mater.*, 2024, **14**, 2304229.

25 H. R. Shin, S. Kim, J. Park, J. H. Kim, M.-S. Park and J.-W. Lee, *Energy Storage Mater.*, 2023, **56**, 515–523.

26 C. Zhang, S. Zhu, D. Wang, C. Lei and Y. Zhao, *J. Energy Storage*, 2023, **73**, 109279.

27 J. Yun, B.-K. Park, E.-S. Won, S. H. Choi, H. C. Kang, J. H. Kim, M.-S. Park and J.-W. Lee, *ACS Energy Lett.*, 2020, **5**, 3108–3114.

28 H. Chen, A. Pei, J. Wan, D. Lin, R. Vilá, H. Wang, D. Mackanic, H.-G. Steinrück, W. Huang, Y. Li, A. Yang, J. Xie, Y. Wu, H. Wang and Y. Cui, *Joule*, 2020, **4**, 938–952.

29 J. Yun, E.-S. Won, H.-S. Shin, K.-N. Jung and J.-W. Lee, *J. Mater. Chem. A*, 2019, **7**, 23208–23215.

30 J. Pu, J. Li, K. Zhang, T. Zhang, C. Li, H. Ma, J. Zhu, P. V. Braun, J. Lu and H. Zhang, *Nat. Commun.*, 2019, **10**, 1896.

31 Y.-X. Zhan, P. Shi, X.-Q. Zhang, F. Ding, J.-Q. Huang, Z. Jin, R. Xiang, X. Liu and Q. Zhang, *Energy Technol.*, 2021, **9**, 2000700.

32 S. Rajendran, A. Sekar and J. Li, *J. Chem. Eng.*, 2024, **484**, 149515.

33 S. Abdul Ahad, J. Drews, T. Danner, A. Latz and H. Geaney, *J. Mater. Chem. A*, 2024, **12**, 12250–12261.

34 W. Huang, Y. Yu, Z. Hou, Z. Liang, Y. Zheng, Z. Quan and Y.-C. Lu, *Energy Storage Mater.*, 2020, **33**, 329–335.

35 S.-H. Hong, D.-H. Jung, J.-H. Kim, Y.-H. Lee, S.-J. Cho, S. H. Joo, H.-W. Lee, K.-S. Lee and S.-Y. Lee, *Adv. Funct. Mater.*, 2020, **30**, 1908868.

36 Y.-X. Zhan, P. Shi, R. Zhang, X.-Q. Zhang, X. Shen, C.-B. Jin, B.-Q. Li and J.-Q. Huang, *Adv. Energy Mater.*, 2021, **11**, 2101654.

37 N.-L. Shen, H. Liu, W.-B. Tang, Z. Liu, T. Wang, Y. Ma, Y. Zhong, J. He, Z. Zhu, Y. Wu and X.-B. Cheng, *Ind. Eng. Chem. Res.*, 2023, **62**, 15360–15377.

38 K. Yan, Z. Lu, H.-W. Lee, F. Xiong, P.-C. Hsu, Y. Li, J. Zhao, S. Chu and Y. Cui, *Nat. Energy*, 2016, **1**, 16010.

39 H. Zhang, X. Liao, Y. Guan, Y. Xiang, M. Li, W. Zhang, X. Zhu, H. Ming, L. Lu, J. Qiu, Y. Huang, G. Cao, Y. Yang, L. Mai, Y. Zhao and H. Zhang, *Nat. Commun.*, 2018, **9**, 3729.

40 E. Cha, J. H. Yun, R. Ponraj and D. K. Kim, *Mater. Chem. Front.*, 2021, **5**, 6294–6314.

41 S. Abdul Ahad, S. Bhattacharya, S. Kilian, M. Ottaviani, K. M. Ryan, T. Kennedy, D. Thompson and H. Geaney, *Small*, 2023, **19**, 2205142.

42 C. Haslam and J. Sakamoto, *J. Electrochem. Soc.*, 2023, **170**, 040524.

43 X. Fei, H. Gao, Y. Xu, W. Ma, B. Yu, F. Tan, G. Cheng and Z. Zhang, *Energy Storage Mater.*, 2024, **65**, 103079.

44 Y. He, M. Zhang, A. Wang, B. Zhang, H. Pham, Q. Hu, L. Sheng, H. Xu, L. Wang, J. Park and X. He, *ACS Appl. Mater.*, 2022, **14**, 33952–33959.

45 D. Petersen, M. Gronenberg, G. Lener, E. P. M. Leiva, G. L. Luque, S. Rostami, A. Paolella, B. J. Hwang, R. Adelung and M. Abdollahifar, *Mater. Horiz.*, 2024, **11**, 5914–5945.

46 Y. Wang, J. Tan, Z. Li, L. Ma, Z. Liu, M. Ye and J. Shen, *Energy Storage Mater.*, 2022, **53**, 156–182.

47 F. Guo, C. Wu, H. Chen, F. Zhong, X. Ai, H. Yang and J. Qian, *Energy Storage Mater.*, 2020, **24**, 635–643.

48 S. Cui, P. Zhai, W. Yang, Y. Wei, J. Xiao, L. Deng and Y. Gong, *Small*, 2020, **16**, 1905620.

49 R. Pathak, Y. Zhou and Q. Qiao, *Appl. Sci.*, 2020, **10**, 4185.

50 E. Kim, W. Choi, S. Ryu, Y. Yun, S. Jo and J. Yoo, *J. Alloys Compd.*, 2023, **966**, 171393.

51 K. Um, C. Jung, H. Nam, H. Lee, S. Yeom and J. H. Moon, *Energy Environ. Sci.*, 2024, **17**, 9112–9121.

52 L. Zhang, H. Zheng, B. Liu, Q. Xie, Q. Chen, L. Lin, J. Lin, B. Qu, L. Wang and D.-L. Peng, *J. Energy Chem.*, 2021, **57**, 392–400.

53 S. Lee, K. su Lee, S. Kim, K. Yoon, S. Han, M. H. Lee, Y. Ko, J. H. Noh, W. Kim and K. Kang, *Sci. Adv.*, 2022, **8**, eabq0153.

54 A. Latz and J. Zausch, *J. Power Sources*, 2011, **196**, 3296–3302.

55 J. Zausch, Fraunhofer Institute for Industrial Mathematics (ITWM), *BEST – Battery and Electrochemistry Simulation Tool*, **https://www.itwm.fraunhofer.de/en/departments/sms/products-services/best-battery-electrochemistry-simulation-tool.html**.

56 S. Hein, T. Danner and A. Latz, *ACS Appl. Energy Mater.*, 2020, **3**, 8519–8531.

57 MathWorks, *MATLAB*, **https://de.mathworks.com/products/matlab.html**.

58 R. Richter, J. Häcker, Z. Zhao-Karger, T. Danner, N. Wagner, M. Fichtner, K. A. Friedrich and A. Latz, *ACS Appl. Energy Mater.*, 2020, **3**, 8457–8474.

59 M. Safari, C. Y. Kwok and L. F. Nazar, *ACS Cent. Sci.*, 2016, **2**, 560–568.

60 S. Wang, J. Qu, F. Wu, K. Yan and C. Zhang, *ACS Appl. Mater.*, 2020, **12**, 8366–8375.

61 Q. Zhang, L. Xu, X. Yue, J. Liu, X. Wang, X. He, Z. Shi, S. Niu, W. Gao, C. Cheng and Z. Liang, *Adv. Energy Mater.*, 2023, **13**, 2302620.

62 Q. Wang, C. Yang, J. Yang, K. Wu, L. Qi, H. Tang, Z. Zhang, W. Liu and H. Zhou, *Energy Storage Mater.*, 2018, **15**, 249–256.

63 B. Zhou, I. Stoševski, A. Bonakdarpour and D. P. Wilkinson, *Adv. Funct. Mater.*, 2023, 2311212.

64 F. Shi, A. Pei, A. Vailionis, J. Xie, B. Liu, J. Zhao, Y. Gong and Y. Cui, *Proc. Natl. Acad. Sci. U. S. A.*, 2017, **114**, 12138–12143.

65 B. Prifling, M. Röding, P. Townsend, M. Neumann and V. Schmidt, *Front. Mater.*, 2021, **8**, 786502.

66 B. Prifling, M. Röding, P. Townsend, M. Neumann and V. Schmidt, *Data set from: Large-scale Statistical Learning for Mass Transport Prediction in Porous Materials Using 90,000 Artificially Generated Microstructures*, Zenodo, DOI: **10.5281/zenodo.4047774**.

67 H. Zhao, D. Lei, Y.-B. He, Y. Yuan, Q. Yun, B. Ni, W. Lv, B. Li, Q.-H. Yang, F. Kang and J. Lu, *Adv. Energy Mater.*, 2018, **8**, 1800266.

68 W. Dong, K. Wang, J. Han, Y. Yu, G. Liu, C. Li, P. Tong, W. Li, C. Yang and Z. Lu, *ACS Appl. Mater.*, 2021, **13**, 8417–8425.

69 B. Park, C. Oh, S. Yu, B. Yang, N. V. Myung, P. W. Bohn and J. L. Schaefer, *J. Electrochem. Soc.*, 2022, **169**, 010511.

70 R. Zhang, N.-W. Li, X.-B. Cheng, Y.-X. Yin, Q. Zhang and Y.-G. Guo, *Adv. Sci.*, 2017, **4**, 1600445.

71 Y. Cheng, J. Chen, Y. Chen, X. Ke, J. Li, Y. Yang and Z. Shi, *Energy Storage Mater.*, 2021, **38**, 276–298.

72 J. Zheng, M. S. Kim, Z. Tu, S. Choudhury, T. Tang and L. A. Archer, *Chem. Soc. Rev.*, 2020, **49**, 2701–2750.

73 S. Zhang, W. Deng, X. Zhou, B. He, J. Liang, F. Zhao, Q. Guo and Z. Liu, *Mater. Today Energy*, 2021, **21**, 100770.